ACS OMEGA

http://pubs.acs.org/journal/acsodf

Article

Auger Electron Spectroscopy Analysis of the Thermally Induced Degradation of $MAPbI_3$ Perovskite Films

Wei-Chun Lin,* Wei-Chun Lo, Jun-Xian Li, Pei-Chen Huang, and Man-Ying Wang

Cite This: *ACS Omega* 2021, 6, 34606−34614

Read Online

ACCESS | Metrics & More | Article Recommendations | Supporting Information

ABSTRACT: Organometal halide perovskites are highly promising materials for photovoltaic applications due to the rapid growth of power conversion efficiency in recent years. However, thermal stability is still a major hurdle for perovskite solar cells toward commercialization. Herein, we first explore the slow thermal response of the $CH_3NH_3PbI_3$ perovskite crystal investigated via Auger electron spectroscopy (AES). AES image mapping directly observes the evolution of morphology and elemental distribution over time. The AES small spot analysis demonstrates the precise initial degradation position of perovskite with both information regarding physical changes in crystals and chemical changes in elemental bonding at the nanometer scale. X-ray photoelectron spectroscopy (XPS) was used to confirm the surface chemical bonding and composition of the perovskite crystals. This work provides the first insights into the physical and chemical changes of perovskites investigated by AES upon long-term exposure to heat under ambient conditions.

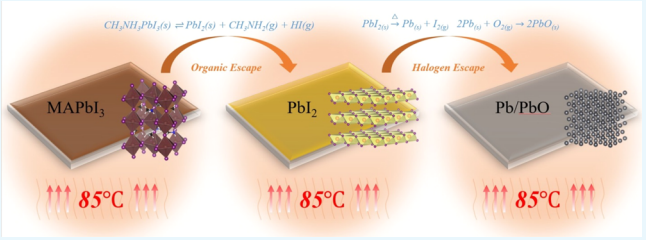

INTRODUCTION

Methylammonium lead iodide ($MAPbI_3$) is one of the promising light-harvesting materials for the next-generation solar cells due to its extraordinary optoelectronic properties, including a high absorption coefficient, long charge carrier diffusion lengths, low exciton binding energy, and a high degree of defect tolerance.[1−4] However, despite achieving laboratory-scale device efficiency comparable to that of commercially available solar cells, perovskite solar cells (PSCs) still retain critical issues regarding stability to different environmental conditions.[5−11] For example, a typical photovoltaic (PV) module available in the market is usually warranted to retain its initial power conversion efficiency for at least 20 years.[12] PSCs are prone to cause material decomposition when devices are exposed to oxygen, UV light, thermal stress (heat), visible light soaking, electric field, or other factors.[13−17] From the perspective of stability concerns, the perovskite PV modules are not ready to fulfill the market requirements before overcoming the degradation factors mentioned above. Hence, an extensive study has recently focused on the full understanding of degradation mechanisms to improve the stability of perovskite solar devices.[18] Stability improvements in devices could be achieved by external encapsulation, adding UV filters, and suppressing trap states for material decomposition caused by oxygen, UV light, and electric fields.[19−23] However, the degradation caused by thermal stress is considered inevitable since it is difficult to avoid the temperature rise of the devices during operation.[24] In an onsite field test, the effective operational temperature could range from −40 to +85 °C, so a standard heat stability test is commonly run within this temperature window.[25]

Typically, device temperatures in higher latitude areas can be increased up to 45 °C, which is higher than ambient temperatures during device operation under direct sunlight.[26] According to the International Standards IEC 61646 climatic chamber tests, long-term thermal stability at 85 °C is required to compete with other types of PV technologies.[27] Therefore, the investigation of the thermal stability of perovskite films has drawn worldwide research attention. Various degradation pathways have been proposed,[11,28−30] and the mechanism remains under debate. As a typical perovskite crystal, the chemical compound of $CH_3NH_3PbI_3$ is usually used as a reference material for studying stability upon exposure to different environmental factors.[28] The $MAPbI_3$ ($CH_3NH_3PbI_3$) crystal clearly loses its excellent light-harvesting properties over time upon exposure to heat. Due to the loss of methylamine iodide (CH_3NH_3I), the perovskite crystal reverts from $MAPbI_3$ ($CH_3NH_3PbI_3$) to lead iodide (PbI_2). The decomposition process is most likely accompanied by a release of gases via common sublimation, as listed in the reactions below.[31] These decomposition byproducts are volatile, making these reactions nearly irreversible. In most of the studies, the heat-induced decomposition process was characterized by X-ray diffraction (XRD), UV−visible spec-

Received: September 10, 2021
Accepted: November 17, 2021
Published: November 29, 2021

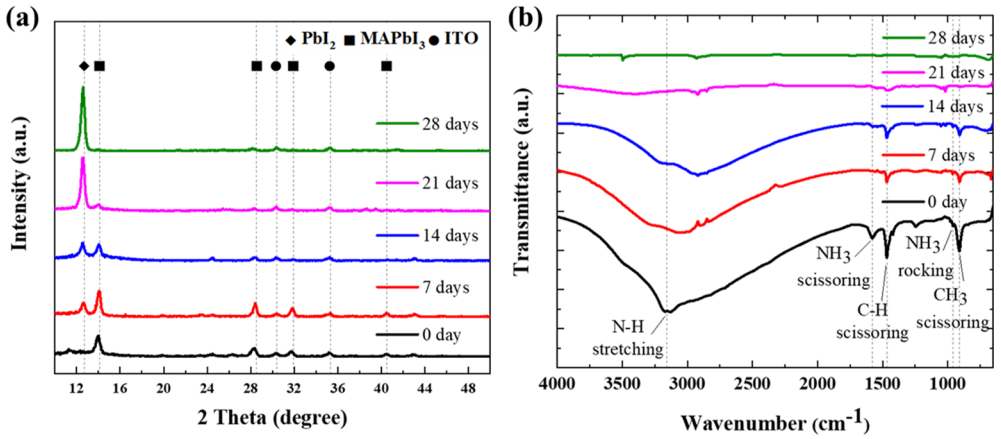

Figure 1. (a) XRD patterns of $MAPbI_3$ with 85 °C heat treatment on a hotplate after 0, 7, 14, 21, and 28 days in the dark. The spectra demonstrate the crystal transformation from $MAPbI_3$ to PbI_2 with heat over time. (b) FTIR spectra of $MAPbI_3$ films with identical heat treatment conditions.

troscopy, and scanning electron microscopy (SEM) to confirm the crystallinity, optical properties, and surface morphology, respectively.[32,33]

$$CH_3NH_3PbI_{3(s)} \rightleftharpoons PbI_{2(s)} + CH_3NH_{2(g)} + HI_{(g)} \quad (1)$$

$$PbI_{2(s)} \xrightarrow{\Delta} Pb_{(s)} + I_{2(g)} \quad (2)$$

$$2Pb_{(s)} + O_{2(g)} \rightarrow 2PbO_{(s)} \quad (3)$$

Recently, X-ray photoelectron spectroscopy (XPS) is used to investigate the compositional change during degradation. Several significant efforts have been directed at analyzing the chemical states and molecular distribution of aged perovskite crystals.[34] On the basis of XPS, surface spectra are used to confirm the oxidation state of each element.[35] However, the field of view depends on the X-ray beam size with several hundred micrometer-scale photoelectron images, which limits the spatial resolution of images. In addition, the surface composition change was examined by XPS rastering the average value over an area of several hundred micrometers, which makes it difficult to address the point-of-interest area at the nanometer scale. In addition, the image quality obtained by XPS also relies on the transfer function of the electromagnetic lens, and the contrast of the resulting image is quite blurry and vague. For this reason, we turned our attention to Auger electron spectroscopy (AES), which is an emerging surface analysis technique for obtaining ultra-high-spatial resolution elemental mapping with small spot analysis. AES has been used to image elemental distribution in numerous applications, such as catalysis, corrosion in steel, adhesion in semiconductor devices, and encapsulation films in the far back end of line.[36−38] From the perspective of the image quality, AES provides an identical secondary electron image as a field emission scanning electron microscope. Moreover, AES provides legible surface information regarding the elemental composition and chemical state of thin solid films, which is feasible to compare the results obtained by XPS. The background theory of AES is accomplished by bombarding a specimen surface with a microfocused electron beam, which facilitates Auger electrons to be produced from the outermost surface of samples (~5 nm). Hence, physical electronics of the Auger instrument provides the ability to capture point spectra with a lateral spatial resolution as small as ~10 nm, which is determined by the electron beam size. Spatial elemental mapping of AES is obtained by scanning the finely focused electron beam across the sample surface, which is useful to address the initial thermal aging position of perovskite in this study. An electron energy analyzer is equipped to measure the kinetic energy of the emitted Auger electrons.[39] From the measured intensity and kinetic energy of an Auger peak, the identification and quantification of a detected element could be determined. Similar to the XPS spectra, chemical-state information is also preserved from the measured Auger peak shape and peak position.

To the best of our knowledge, AES has not been used to investigate perovskite films. Carbon, nitrogen, and lead are the three primary elements for compositional analysis during the decomposition process of perovskite crystals. In this study, XPS was used as a primary tool to investigate the surface composition change and the chemical state of the perovskite films over a large area (~200 × 200 μm^2) upon exposure to heat (85 °C). Therefore, small spot analysis from AES is necessary for obtaining information regarding the initial decomposition position of thermally induced degradation. Furthermore, scanning electron images with *in situ* AES mapping were used to observe the elemental distribution of perovskite films in high spatial resolution. The corresponding point spectra provide composition analysis in the nanometer-scale range, which is sufficient to target the specific area (aging position) from the secondary electron image. In summary, nitrogen concentration significantly decreased after 21 days of heat treatment. The orientation of the perovskite crystal was distorted from a dense and coarse-grained crystal to a needle structure with plenty of holes. The AES point spectra (small spot analysis) show the decomposition process on each element. In addition to elemental distribution, long-term heat treatment also causes oxidation of lead. Time-of-flight secondary ion mass spectrometry (ToF-SIMS) was used to confirm the formation of lead oxide. All surface analysis results confirm the formation of lead oxide and the escape of ammonia and methyl iodide during the decomposition process of perovskite upon exposure to heat.

RESULTS AND DISCUSSION

The crystallinity and structural degradation of the perovskite film can be analyzed by XRD, as shown in Figure 1a. The fresh perovskite specimen (0 day) was exposed to an 85 °C hot plate for different durations. In XRD measurements, $MAPbI_3$ peaks

https://doi.org/10.1021/acsomega.1c05002
ACS Omega 2021, 6, 34606−34614

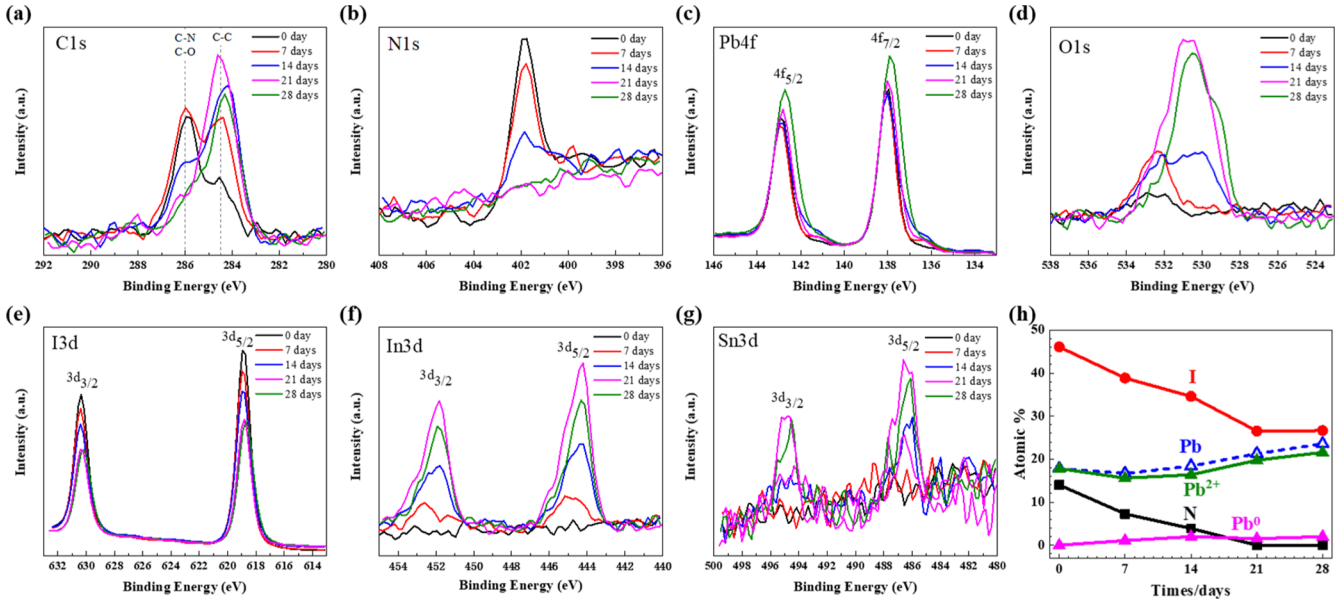

Figure 2. XPS spectra of the $MAPbI_3$ films with different aging durations: (a) C 1s, (b) N 1s, (c) Pb 4f, (d) O 1s, (e) I 3d, (f) In 3d and (g) Sn 3d. All peaks are calibrated using C 1s (284.8 eV). (h) Surface composition of $MAPbI_3$ over time.

Table 1. XPS Surface Composition of Heat-Induced Degradation $MAPbI_3$ Samples (Relative Atom %)

	C 1s	N 1s	O 1s	Pb 4f	I 3d5	In 3d5	Sn 3d
0 days	18.84	14.00	3.25	17.82	46.08	<0.1	<0.1
7 days	28.61	7.29	7.45	16.67	38.86	1.13	<0.1
14 days	28.05	3.90	12.22	18.38	34.59	2.51	0.35
21 days	26.49	<0.1	22.67	18.71	26.54	4.78	0.82
28 days	24.04	<0.1	22.05	23.23	26.65	3.41	0.63

are observed at 14.02, 28.32, 31.72, and 40.48°, which are assigned to the (1 0 0), (2 0 0), (2 1 0), and (2 2 0) planes, respectively. The peak appearing at 12.71° can be assigned as the (0 0 1) plane due to the formation of the PbI_2 crystal, which indicates that the crystal structure of the perovskite film started to change over time until it was completely converted into PbI_2 after 28 days. To investigate the differences in the organic compounds during degradation, Fourier transform infrared (FT-IR) spectroscopy was performed before and after heat treatment. As demonstrated in Figure 1b, the characteristic vibrational bands of methylammonium are identified. The bands are assigned to CH_3 scissoring at 910 cm^{-1}; C−H scissoring at 1465 cm^{-1} for the methyl functional groups; NH_3 rocking at 960 cm^{-1}; NH_3 scissoring at 1580 cm^{-1}; and N−H stretching at 3160 cm^{-1} for the ammonium functional groups. The ammonium bands at 960, 1580, and 3160 cm^{-1} after 21 days entirely disappeared; in contrast, the methyl bands at 910 and 1580 cm^{-1} disappeared until 28 days. The FTIR results show that the ammonium functional groups escaped faster than methyl functional groups, which is consistent with the literature reported by Abdelmageed et al.[40]

To observe the intrinsic degradation of the perovskite films, the elemental composition of the samples was further examined by XPS. Figure 2a−g demonstrates the XPS spectra of C 1s, N 1s, Pb 4f, O 1s, I 3d, In 3d, and Sn 3d from $MAPbI_3$ samples with various heat treatment durations. The fresh C 1s core levels (0 day, black curve) displayed the main peak at 286 eV, which represents the C−N bond of perovskite. The other peak is observed at 284.8 eV and represents the C−C bond of perovskite and surface contamination. It is obvious that the intensity of the C−N bond gradually decreased and formed more C−C bonds with increasing heating time (Figure 2a).[41] For the samples containing organic compounds, the N 1s core levels appear at 401.8 eV (Figure 2b). The intensity of nitrogen decreased with time until 14 days and without a nitrogen signal after 21 days of heat treatment. This XPS result is consistent with the XRD and FTIR data in Figure 1 and can be explained by reaction 1, which indicates the formation of lead iodide and volatile methylamine and hydrogen iodide. The Pb 4f spectra show that a small metallic lead (Pb^{0+}) peak was formed at ∼136.5 eV after 7 days of heat treatment (Figure 2c). Interestingly, the Pb^{0+} peak does not increase over time. The reason may be due to the formation of lead oxide when the specimen was further heated under ambient conditions. The O 1s spectra in Figure 2d confirm that the organic C−O bond (∼533 eV) shifted to metallic oxides (∼529.5 eV) with increasing heating time. Decreasing I 3d spectra are observed over time and prove the escape of iodine in the chemical reaction 2 below (Figure 2e). The Pb 4f, O 1s, and I 3d spectra confirm that chemical reactions 2 and 3 further facilitate the decomposition of the perovskite crystals. Figure 2f,g illustrates the ITO substrate information regarding the In 3d and Sn 3d XPS spectra for confirming the coverage of the perovskite films. It was found that a longer heating time leads to a stronger intensity for both signals. The compositional evolution (relative atomic concentration) of I, N, Pb^{2+}, and Pb^0 on the $MAPbI_3$ film surface over the heating durations is shown in Figure 2h. The initial elemental ratio (N/Pb/I) of fresh $MAPbI_3$ was 1:1.27:3.29, that is, close to the original stoichiometric value. The slightly higher amount of iodine in

https://doi.org/10.1021/acsomega.1c05002
ACS Omega 2021, 6, 34606−34614

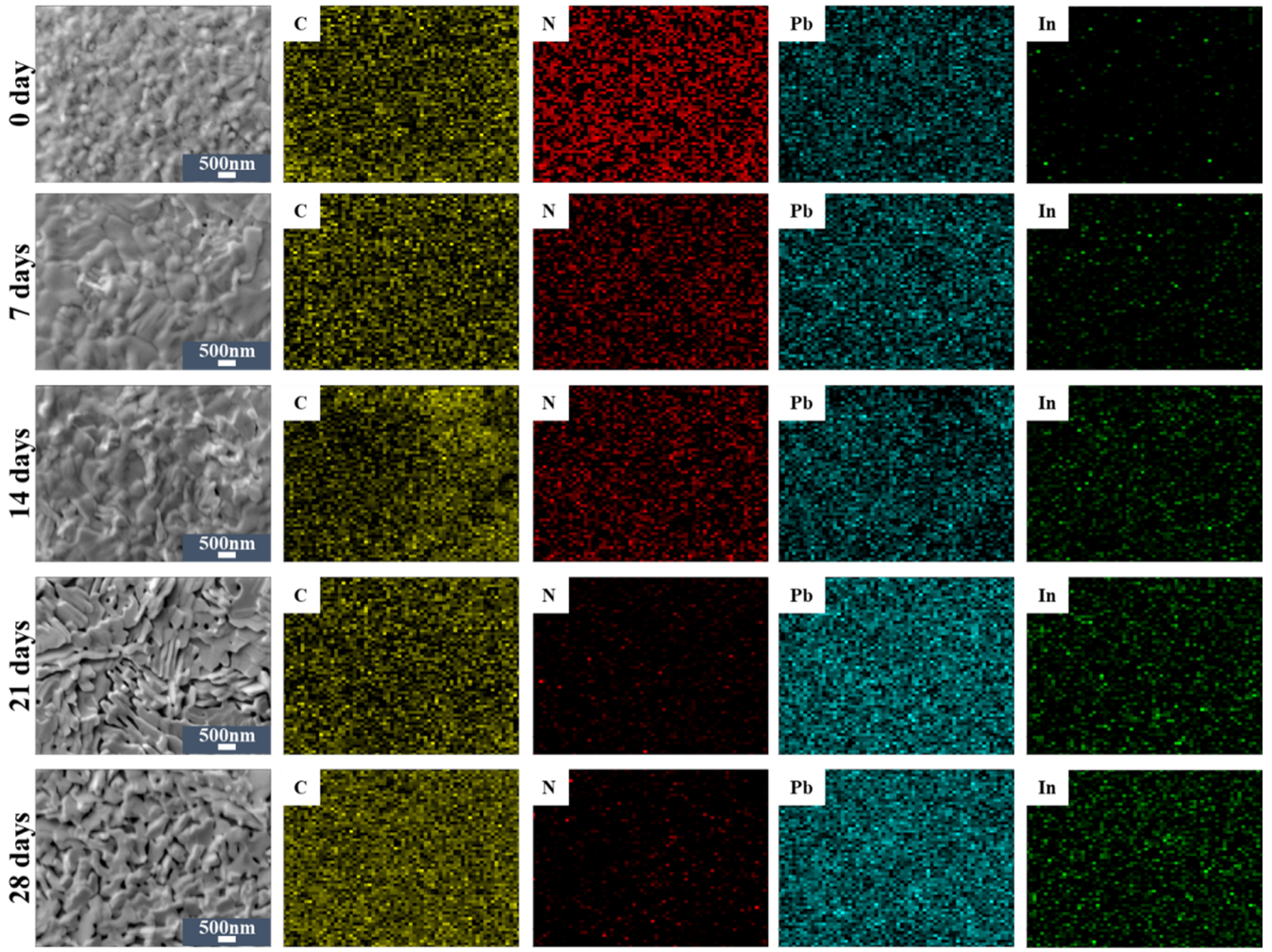

Figure 3. Elemental distribution of $MAPbI_3$ thin films with different aging times measured by AES. The corresponding SEM images (scale bar: 500 nm) are also given ahead of the elemental mapping.

the surface sensitivity measurement could be attributed to the residual methylammonium iodide (MAI) present on the surface due to the sequential preparation of the perovskite film. The atomic ratio of nitrogen and iodine decreases with increasing heating time. Table 1 shows the comprehensive composition of the ITO/$MAPbI_3$ specimen with different heating times. The ratios of oxygen, lead, indium, and tin continued to rise during the decomposition process. The XPS result confirms that reaction 2 is an intermediate state of heat-induced degradation, and the $MAPbI_3$ crystal eventually becomes solid PbI_2 and PbO.

The 2D elemental distribution of $MAPbI_3$ at ∼5 nm depths was first investigated via the AES, which reflected the atomic concentration of each primary element, as shown in Figure 3. The Auger O KLL spectrum overlaps with the I MNN, as shown in Figure S1, so these two elements were excluded from Figure 3. The SEM image of the fresh perovskite film (aged 0 days) shows dense and compact grains. The C KLL, N KLL, and Pb NOO spectra are distributed uniformly on the surface without the indium MNN signal, which reveals the fresh $MAPbI_3$ film. Few indium sparkles in the 0-day sample can be treated as noise, as confirmed by the AES In spectrum in Figure S1. After 7 days of heat treatment, the grains become larger, with few cracks and pinholes. The intensity of the nitrogen mapping was significantly reduced; on the other hand, the indium signal slightly increased. The distribution of carbon and lead remained similar to that of the fresh sample. From the SEM image in Figure 3, it is observed that the perovskite becomes highly disordered and the crystal is distorted by the 14-day heat treatment. Interestingly, the carbon and lead distributions are found to be complementary to each other. This phenomenon is due to the loss of methylammonia and the formation of lead iodine. The nitrogen distribution continues to become scarce, and the indium signal becomes densified. After the sample is aged for 21 days, the surface morphology of the perovskite crystal is elongated and significantly altered to a flake structure with a large gap between grain boundaries. Carbon and nitrogen are distributed thinner, and lead and indium are distributed densely and more uniformly. The flake-structured crystals further grew with a continuous grain network after 28 days of aging. The long-term heat treatment provides driving energy for the recrystallization process. In this stage, most of the organic compounds disappeared, and $PbI_{2(s)}$, $Pb_{(s)}$ and $PbO_{(s)}$ are residues on the ITO substrate (reactions 1−3). Therefore, the distribution of C and Pb became uniform again. The uniform C distribution is due to the surface carbonization after long-term exposure to heat.

To observe the elemental change in a specific region during degradation, small spot analysis of the Auger spectrum was

https://doi.org/10.1021/acsomega.1c05002
ACS Omega 2021, 6, 34606−34614

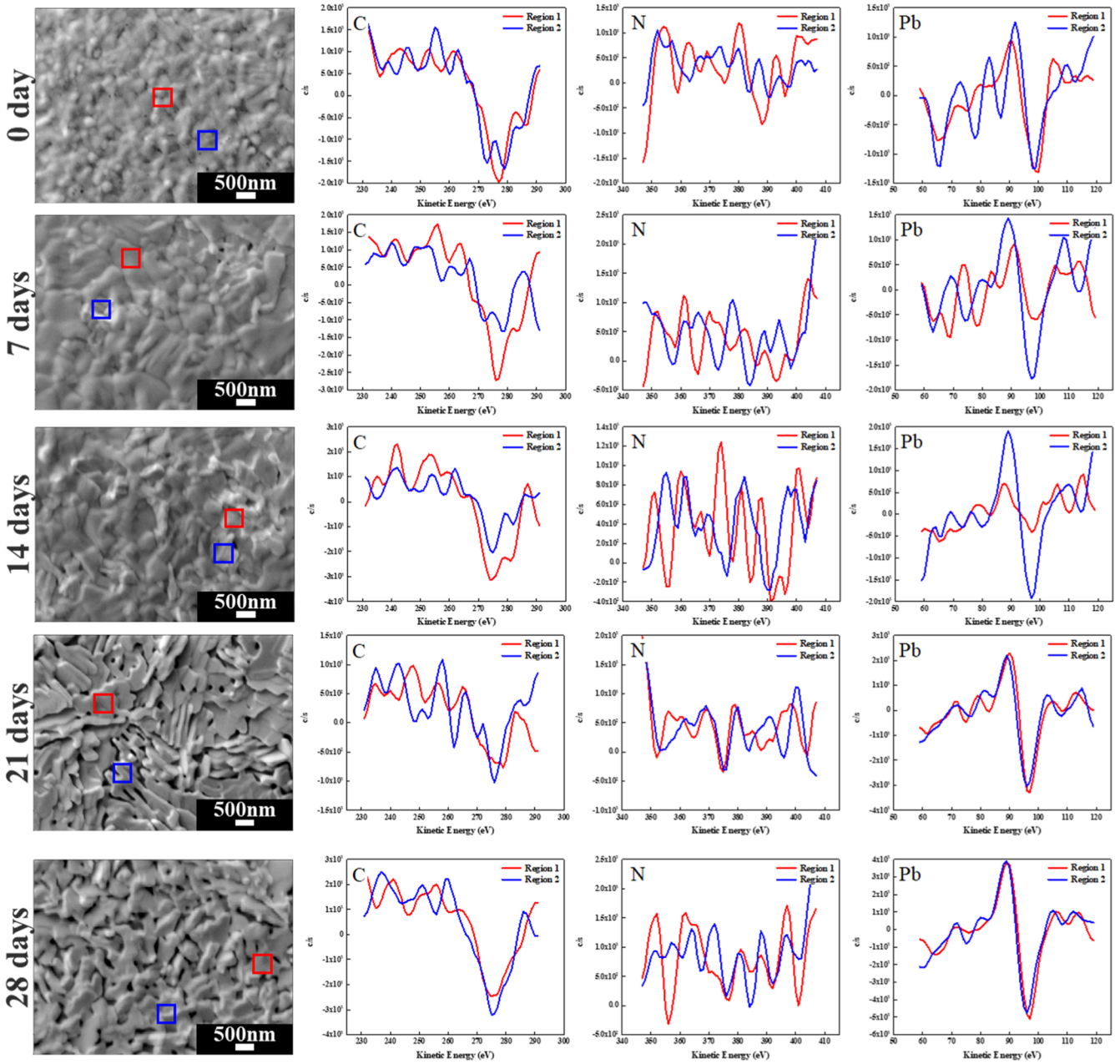

Figure 4. AES small spot analysis of $MAPbI_3$ thin films with different aging times. The corresponding SEM images (scale bar: 500 nm) are also given ahead of the elemental mapping.

used to explore the aging source among the grains. SEM imaging combined with an Auger spectroscopic study of grain changes during different degradation periods is shown in Figure 4. For the elemental fine scan on the perovskite film, two regions of interest (ROIs) are selected (area 500 nm × 500 nm) in each specimen. Based on the observation from the elemental mapping in Figure 3, one of the normal grains was selected for elemental scanning and marked as the ROI red square; the other blue square was selected due to distortion of the surface morphology. The AES spectra of carbon and lead on the fresh sample (0 day) demonstrated that both ROI regions contain similar elemental signal intensities without significant differences. The nitrogen spectrum is weak for AES, which is due to the limited escape depth of the corresponding Auger electron. After seven days of aging, the carbon signal from the red ROI remained similar to that of the fresh sample. The blue ROI of the 7-day sample reveals the Auger spectra on the distorted grains, which contain less carbon and a greater lead signal than the red ROI. The result indicates that this region is degraded due to the escape of volatile CH_3NH_2 and HI, leaving the lead iodide solid on the substrate. This result demonstrates for the first time the chemical change of the initial aging region of perovskite film on the nanometer scale. After 14 days, the blue region contains less carbon and a strong lead signal. From the SEM image, this area undergoes structural alteration by the rapid loss of organic compounds and will turn into a flake-shaped structure. The samples aged for 21 and 28 days underwent recrystallization with totally different surface morphologies compared to those of samples in the previous three stages. The intensity of each elemental spectrum is similar on the sample, which indicates that heat-induced decomposition is the primary focus of reactions 2 and

https://doi.org/10.1021/acsomega.1c05002
ACS Omega 2021, 6, 34606−34614

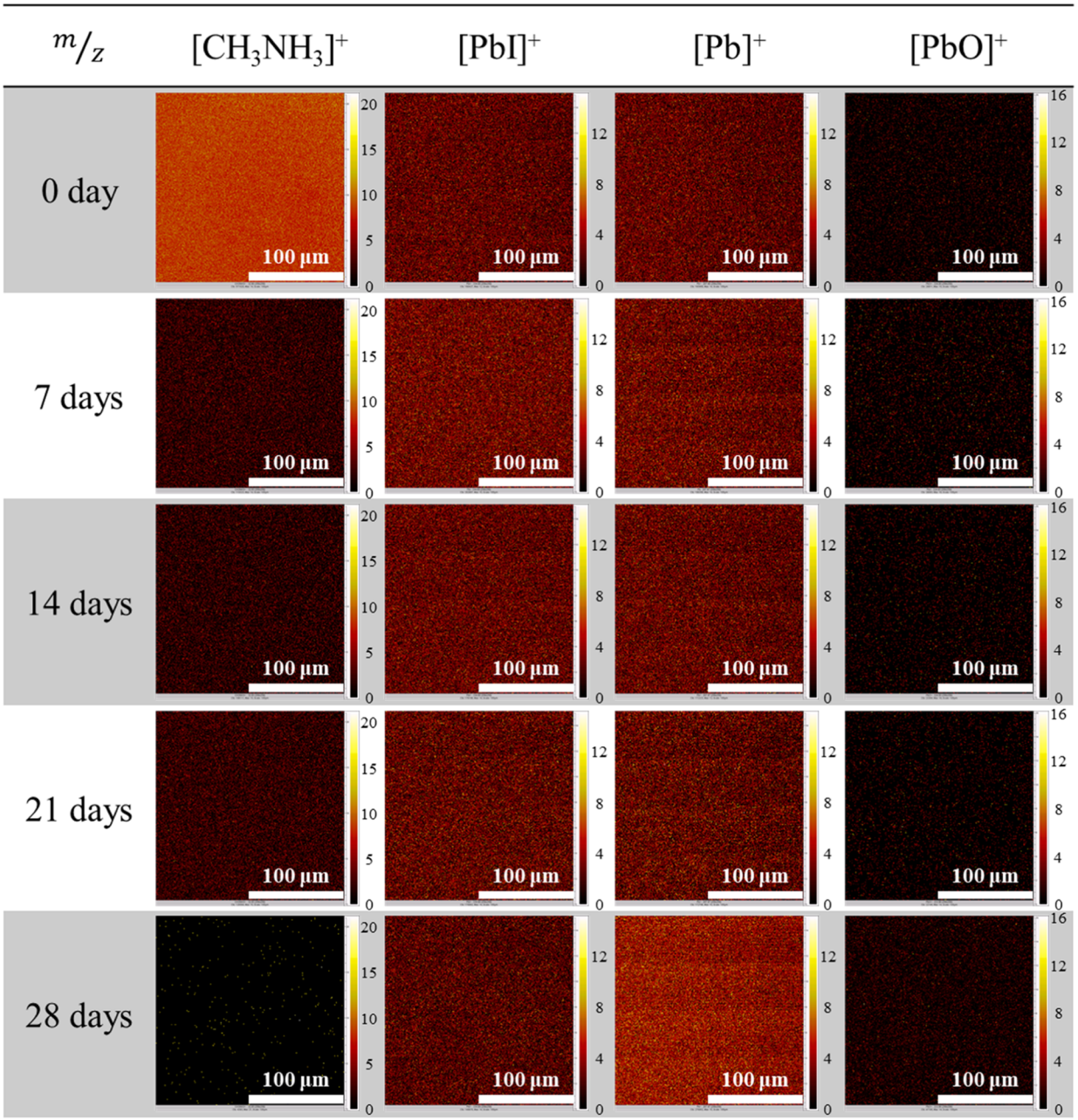

Figure 5. ToF-SIMS positive ion images demonstrate the evolution of each molecule over various aging times. The color map illustrates the molecular density from high (light yellow) to low (black).

3 at these stages. In summary, the AES elemental spectra proved that the regional decomposition position was usually accompanied by structural distortion of the perovskite crystals. The AES elemental mapping results are consistent with the XPS composition study. Small spot analysis combined with secondary electron images provides an opportunity to observe the chemical change from the degradation source.

To verify the degradation mechanism, ToF-SIMS analysis was used to investigate the decomposed molecules in reactions 2 and 3. Figure 5 shows a series of 2D ToF-SIMS images, which illustrate the ion distribution for the specimen with different aging durations. The positive $[CH_3NH_3]^+$ ions are used to observe the evolution of organic compounds in $MAPbI_3$ during the decomposition process. The weakening distribution of $[CH_3NH_3]^+$ (from bright to dark) over time proves the disappearance of the organic compound in reaction 1. This result is consistent with the nitrogen intensity in XPS and nitrogen mapping in AES. The $[PbI]^+$ and $[Pb]^+$ ions are indicators for the formation of $Pb_{(s)}$ and $I_{(g)}$ in reaction 2. Interestingly, the intensity of $[PbI]^+$ increased for the 7- and 14-days heat treatments. After that, the color map of the $[PbI]^+$ molecule becomes darker. The rise and fall of the $[PbI]^+$ intensity prove that the PbI_2 in reaction 1 is further decomposed to $Pb_{(s)}$ and $I_{(g)}$. This result could be confirmed by the increasing intensity of $[Pb]^+$ molecules over time. The increasing intensity of the $[PbO]^+$ molecule verifies the oxidation of lead after long-term exposure to heat.

CONCLUSIONS

Using XRD, FTIR, XPS, AES, and ToF-SIMS, $CH_3NH_3PbI_3$ perovskite films were analyzed after being exposed to 85 °C

https://doi.org/10.1021/acsomega.1c05002
ACS Omega 2021, 6, 34606−34614

under dark ambient conditions for variable times. Chemical degradation was observed via XPS spectra (C 1s and N 1s), indicating the rapid loss of methylammonium. In addition, we show the formation of PbO after long-term exposure to heat under ambient conditions. The good agreement between AES mapping and other analysis techniques indicates that the AES analysis provides high-spatial resolution elemental mapping, which is adequate for analyzing the compositional distribution in such hybrid films. In this study, we introduce AES small spot analysis to investigate the region of aging initiation of perovskite crystals. It is directly observed that the loss of organic compounds could be addressed by AES point spectral analysis (area ~ 500 nm^2). The ToF-SIMS results confirm the observation from XPS and AES, which indicates that the sublimation of methylamine is the key factor for the $CH_3NH_3PbI_3$ crystals reverting to PbI_2. Metallic lead was also found after long-term heat treatment, which eventually resulted in the formation of lead oxide. In this article, three primary surface analysis techniques are used together for the first time to investigate the heat-induced degradation of perovskite crystals. These three surface analysis techniques help visualize the degradation process of perovskite crystals from different perspectives, which opens a window to further investigate perovskite-based materials in various applications.

EXPERIMENTAL SECTION

Perovskite Fabrication. ITO-based perovskite samples were fabricated only with $MAPbI_3$ thin film on top of ITO. The hole transport layer was removed for simpler observation of heat-induced degradation. The ITO substrate was cleaned under a sonicator with a solution of cleaning detergent, DI water, acetone, and isopropanol for 15 min each. The substrate was then dried with flowing N_2 and stored in an oven at 85 °C overnight. The PbI_2 precursor solution was prepared by dissolving 460 mg/mL in *N*,*N*-dimethylformamide at a concentration of 1 M and kept at 70 °C overnight. Then, 40 mg of methylamine iodide (CH_3NH_3I) was dissolved in 1 mL of isopropanol at room temperature.

The dried ITO substrates were cleaned by UV ozone for 15 min before use. The $MAPbI_3$ thin film was deposited on a cleaned ITO substrate by a two-step process. The PbI_2 solution was spin coated on the ITO substrate at 6000 rpm for 30 s and then annealed at 70 °C for 10 min under ambient conditions. The resulting MAI solutions were dropped onto the substrates, and then the samples were spun at 8000 rpm for 10 s, followed by annealing at 100 °C for 10 min. To observe the heat-induced degradation of the perovskite films, the samples were heated on a glass Petri dish at 85 °C in an ambient environment for various durations. The Petri dish was covered with an aluminum foil to prevent light soaking. Another batch of samples was stored under the same conditions except for the heat as the reference specimen.

Characterization. The crystal structure and stability of the perovskite films were determined by XRD analysis with a Cu Kα radiation source (Bruker D8 Advance instrument). XRD pattern parameters were collected from 10 to 50° 2θ, with a step size of 0.04°/step and a counting time of 1.2 s/step. FTIR spectroscopy (PerkinElmer Frontier) was used to characterize the functional groups of methyl and amino groups to investigate the heat-induced decomposition of perovskite thin films. Various degradation durations were performed at wavenumbers of 4000−650 cm^{-1}.

The surface chemistry was carried out with an XPS system. XPS spectra were recorded with a PHI 5000 VersaProbe system (ULVAC-PHI, Chigasaki, Japan). Microfocused Al Kα X-ray (25 W, 100 μm) and the analyzer were rastered on an area of 300 × 300 μm^2. The take-off angle of the photoelectron was fixed at 45°. A dual-beam charge neutralizer was used for charge compensation.

AES elemental maps were collected using a multichannel detector with a cylindrical mirror analyzer on a Phi 690 scanning Auger NanoProbe system using a field emission electron gun at 3 kV and 5 nA. A scintillator was used for secondary electron imaging. The stage supporting the sample was tilted at 45° to avoid any charging effect. The main chamber was maintained under vacuum ~3 × 10^{-6} Pa. 2D elemental maps were obtained by scanning Auger microscopy (SAM). Due to the smaller interaction volumes and the short escape depth of the Auger effect, the analysis depth of the SAM is ~5 nm. Using the characteristics of the Auger spectrum with small spot high spatial resolution images could be obtained based on the characteristics mentioned above.

ToF-SIMS images were acquired using a PHI TRIFT V nanoTOF (ULVAC-PHI, Japan) system. A pulsed C_{60}^+ (approximately 8200 Hz with 15 ns pulse length) rastering over a 200 μm × 200 μm area was applied as the primary ion beam. C_{60}^+ ions were applied due to the lower accumulation of surface damage, which was validated in a previous study.[42] The acceleration voltage of the incident C_{60}^+ ion was 20 kV, and the beam current was 0.08 nA-DC. The acquisition time was 10 min for each image, so a desirable image contrast was obtained with the ion dosage beneath the static limit.

ASSOCIATED CONTENT

Supporting Information

The Supporting Information is available free of charge at https://pubs.acs.org/doi/10.1021/acsomega.1c05002.

Illustration of the electron images of the specimen with different aging durations with the corresponding small spot analysis of In, O, and I spectra and counts of each ion image obtained from ToF-SIMS (PDF)

AUTHOR INFORMATION

Corresponding Author

Wei-Chun Lin − *Department of Photonics, National Sun Yat-Sen University, Kaohsiung City 804, Taiwan (ROC); Department of Materials Science and Engineering, Feng Chia University, Taichung City 407802, Taiwan (ROC);* orcid.org/0000-0001-5722-6383; Email: wclin@mail.nsysu.edu.tw

Authors

Wei-Chun Lo − *Department of Photonics, National Sun Yat-Sen University, Kaohsiung City 804, Taiwan (ROC); Department of Materials Science and Engineering, Feng Chia University, Taichung City 407802, Taiwan (ROC)*

Jun-Xian Li − *Department of Photonics, National Sun Yat-Sen University, Kaohsiung City 804, Taiwan (ROC); Department of Materials Science and Engineering, Feng Chia University, Taichung City 407802, Taiwan (ROC)*

Pei-Chen Huang − *Department of Photonics, National Sun Yat-Sen University, Kaohsiung City 804, Taiwan (ROC)*

Man-Ying Wang − *Department of Photonics, National Sun Yat-Sen University, Kaohsiung City 804, Taiwan (ROC)*

https://doi.org/10.1021/acsomega.1c05002
ACS Omega 2021, 6, 34606−34614

Complete contact information is available at:
https://pubs.acs.org/10.1021/acsomega.1c05002

Notes

The authors declare no competing financial interest.

■ ACKNOWLEDGMENTS

The authors acknowledge sponsorship by the Ministry of Science and Technology through grant number MOST 108-2113-M-035-002-MY2 and MOST 110-2113-M-110-024. The authors acknowledge instrument support from RCAS, Academia Sinica.

■ REFERENCES

(1) Sun, S.; Salim, T.; Mathews, N.; Duchamp, M.; Boothroyd, C.; Xing, G.; Sum, T. C.; Lam, Y. M. The Origin of High Efficiency in Low-Temperature Solution-Processable Bilayer Organometal Halide Hybrid Solar Cells. *Energy Environ. Sci.* **2014**, *7*, 399−407.
(2) Stranks, S. D.; Alcocer, M. J. P.; Leijtens, T.; Herz, L. M.; Petrozza, A.; Snaith, H. J. Electron-Hole Diffusion Lengths Exceeding Trihalide Perovskite Absorber. *Science* **2013**, *342*, 341−344.
(3) Chen, X.; Lu, H.; Yang, Y.; Beard, M. C. Excitonic Effects in Methylammonium Lead Halide Perovskites. *J. Phys. Chem. Lett.* **2018**, *9*, 2595−2603.
(4) Wang, L.; Yuan, G. D.; Duan, R. F.; Huang, F.; Wei, T. B.; Liu, Z. Q.; Wang, J. X.; Li, J. M. Tunable Bandgap in Hybrid Perovskite CH3NH3Pb(Br3-YXy) Single Crystals and Photodetector Applications. *AIP Adv.* **2016**, *6*, 045115.
(5) Wang, D.; Wright, M.; Elumalai, N. K.; Uddin, A. Stability of Perovskite Solar Cells. *Sol. Energy Mater. Sol. Cells* **2016**, *147*, 255−275.
(6) Wali, Q.; Iftikhar, F. J.; Khan, M. E.; Ullah, A.; Iqbal, Y.; Jose, R. Advances in Stability of Perovskite Solar Cells. *Org. Electron.* **2020**, *78*, 105590.
(7) Arabpour Roghabadi, F.; Alidaei, M.; Mousavi, S. M.; Ashjari, T.; Tehrani, A. S.; Ahmadi, V.; Sadrameli, S. M. Stability Progress of Perovskite Solar Cells Dependent on the Crystalline Structure: From 3D ABX3 to 2D Ruddlesden-Popper Perovskite Absorbers. *J. Mater. Chem. A* **2019**, *7*, 5898−5933.
(8) Boyd, C. C.; Cheacharoen, R.; Leijtens, T.; McGehee, M. D. Understanding Degradation Mechanisms and Improving Stability of Perovskite Photovoltaics. *Chem. Rev.* **2019**, *119*, 3418−3451.
(9) Kumar, A.; Bansode, U.; Ogale, S.; Rahman, A. Understanding the Thermal Degradation Mechanism of Perovskite Solar Cells via Dielectric and Noise Measurements. *Nanotechnology* **2020**, *31*, 365403−365413.
(10) Li, B.; Li, Y.; Zheng, C.; Gao, D.; Huang, W. Advancements in the Stability of Perovskite Solar Cells: Degradation Mechanisms and Improvement Approaches. *RSC Adv.* **2016**, *6*, 38079−38091.
(11) Bisquert, J.; Juarez-Perez, E. J. The Causes of Degradation of Perovskite Solar Cells. *J. Phys. Chem. Lett.* **2019**, *10*, 5889−5891.
(12) Wang, D.; Wright, M.; Elumalai, N. K.; Uddin, A. Stability of Perovskite Solar Cells. *Sol. Energy Mater. Sol. Cells* **2016**, *147*, 255.
(13) Wang, C.; Li, Y.; Xu, X.; Wang, C.; Xie, F.; Gao, Y. Degradation of Co-Evaporated Perovskite Thin Film in Air. *Chem. Phys. Lett.* **2016**, *649*, 151−155.
(14) Sun, Y.; Fang, X.; Ma, Z.; Xu, L.; Lu, Y.; Yu, Q.; Yuan, N.; Ding, J. Enhanced UV-Light Stability of Organometal Halide Perovskite Solar Cells with Interface Modification and a UV Absorption Layer. *J. Mater. Chem. C* **2017**, *5*, 8682−8687.
(15) Yang, H.; Mamun, A. A.; Marsillac, S. A Facile Way to Improve the Performance of Perovskite Solar Cells by Toluene and Diethyl Ether Mixed Anti-Solvent Engineering. *Coatings* **2019**, *9*, 766.
(16) Zhang, Y.; Wang, P.; Yu, X.; Xie, J.; Sun, X.; Wang, H.; Huang, J.; Xu, L.; Cui, C.; Lei, M.; Yang, D. Enhanced Performance and Light Soaking Stability of Planar Perovskite Solar Cells Using an Amine-Based Fullerene Interfacial Modifier. *J. Mater. Chem. A* **2016**, *4*, 18509−18515.
(17) Bae, S.; Kim, S.; Lee, S.-W.; Cho, K. J.; Park, S.; Lee, S.; Kang, Y.; Lee, H.-S.; Kim, D. Electric-Field-Induced Degradation of Methylammonium Lead Iodide Perovskite Solar Cells. *J. Phys. Chem. Lett.* **2016**, *7*, 3091−3096.
(18) Sandeep Kumar, G.; Kanti Sarkar, P.; Pradhan, B.; Hossain, M.; Rao, D. M.; Acharya, S. Large-Area Transparent Flexible Guanidinium Incorporated $MAPbI_3$ Microstructures for High-Performance Photodetectors with Enhanced Stability. *Nanoscale Horiz.* **2020**, *5*, 696.
(19) Matteocci, F.; Cinà, L.; Lamanna, E.; Cacovich, S.; Divitini, G.; Midgley, P. A.; Ducati, C.; Di Carlo, A. Encapsulation for Long-Term Stability Enhancement of Perovskite Solar Cells. *Nano Energy* **2016**, *30*, 162−172.
(20) Aljaiuossi, G.; Makableh, Y. F.; Al-Fandi, M. Design and Optimization of Nanostructured UV-Filters for Efficient and Stable Perovskite Solar Cells. *Semicond. Sci. Technol.* **2019**, *34*, 125014.
(21) Poorkazem, K.; Kelly, T. L. Improving the Stability and Decreasing the Trap State Density of Mixed-Cation Perovskite Solar Cells through Compositional Engineering. *Sustainable Energy Fuels* **2018**, *2*, 1332−1341.
(22) Arabpour Roghabadi, F.; Mansour Rezaei Fumani, N.; Alidaei, M.; Ahmadi, V.; Sadrameli, S. M. High Power UV-Light Irradiation as a New Method for Defect Passivation in Degraded Perovskite Solar Cells to Recover and Enhance the Performance. *Sci. Rep.* **2019**, *9*, 9448.
(23) Wang, W.-T.; Chen, P.; Chiang, C. H.; Guo, T. F.; Wu, C. G.; Feng, S. P. Synergistic Reinforcement of Built-In Electric Fields for Highly Efficient and Stable Perovskite Photovoltaics. *Adv. Funct. Mater.* **2020**, *30*, 1909755.
(24) Yang, W.; Zhong, D.; Shi, M.; Qu, S.; Chen, H. Toward Highly Thermal Stable Perovskite Solar Cells by Rational Design of Interfacial Layer. *iScience* **2019**, *22*, 534−543.
(25) Cheacharoen, R.; Boyd, C. C.; Burkhard, G. F.; Leijtens, T.; Raiford, J. A.; Bush, K. A.; Bent, S. F.; McGehee, M. D. Encapsulating Perovskite Solar Cells to Withstand Damp Heat and Thermal Cycling. *Sustainable Energy Fuels* **2018**, *2*, 2398−2406.
(26) Sze, S. M.; Ng, K. K. *Physics of Semiconductor Devices*; John Wiley & Sons, 2006.
(27) Cincinnati Sub-Zero Industrial. *Photovoltaic Module & Solar Panel Environmental Testing Guide*, 2016; pp 1−12.
(28) Boyd, C. C.; Cheacharoen, R.; Leijtens, T.; McGehee, M. D. Understanding Degradation Mechanisms and Improving Stability of Perovskite Photovoltaics. *Chem. Rev.* **2018**, *119*, 3418−3451.
(29) Dunfield, S. P.; Bliss, L.; Zhang, F.; Luther, J. M.; Zhu, K.; van Hest, M. F. A. M.; Reese, M. O.; Berry, J. J. From Defects to Degradation: A Mechanistic Understanding of Degradation in Perovskite Solar Cell Devices and Modules. *Adv. Energy Mater.* **2020**, *10*, 1904054.
(30) Zhang, C. X.; Shen, T.; Guo, D.; Tang, L. M.; Yang, K.; Deng, H. X. Reviewing and Understanding the Stability Mechanism of Halide Perovskite Solar Cells. *InfoMat* **2020**, *2*, 1034−1056.
(31) Juarez-Perez, E. J.; Ono, L. K.; Maeda, M.; Jiang, Y.; Hawash, Z.; Qi, Y. Photodecomposition and Thermal Decomposition in Methylammonium Halide Lead Perovskites and Inferred Design Principles to Increase Photovoltaic Device Stability. *J. Mater. Chem. A* **2018**, *6*, 9604−9612.
(32) Zhang, H.; Ren, X.; Chen, X.; Mao, J.; Cheng, J.; Zhao, Y.; Liu, Y.; Milic, J.; Yin, W.-J.; Grätzel, M.; Choy, W. C. H. Improving the Stability and Performance of Perovskite Solar Cells: Via off-the-Shelf Post-Device Ligand Treatment. *Energy Environ. Sci.* **2018**, *11*, 2253−2262.
(33) Dao, Q.-D.; Tsuji, R.; Fujii, A.; Ozaki, M. Study on Degradation Mechanism of Perovskite Solar Cell and Their Recovering Effects by Introducing CH3NH3I Layers. *Org. Electron.* **2017**, *43*, 229−234.
(34) Ginting, R. T.; Jeon, M.-K.; Lee, K.-J.; Jin, W.-Y.; Kim, T.-W.; Kang, J.-W. Degradation Mechanism of Planar-Perovskite Solar Cells: Correlating Evolution of Iodine Distribution and Photocurrent Hysteresis. *J. Mater. Chem. A* **2017**, *5*, 4527−4534.

(35) McGettrick, J. D.; Hooper, K.; Pockett, A.; Baker, J.; Troughton, J.; Carnie, M.; Watson, T. Sources of Pb(0) Artefacts during XPS Analysis of Lead Halide Perovskites. *Mater. Lett.* **2019**, *251*, 98.
(36) Radvanyi, E.; De Vito, E.; Porcher, W.; Danet, J.; Desbois, P.; Colin, J.-F.; Si Larbi, S. J. Study of Lithiation Mechanisms in Silicon Electrodes by Auger Electron Spectroscopy. *J. Mater. Chem. A* **2013**, *1*, 4956−4965.
(37) Abadie, L. M.; Chamorro, J. M. Analytical Solutions. *Lect. Notes Energy* **2013**, *21*, 45−76.
(38) Si, S. *Full Wafer Particle Analysis of Sub-50 nm Defects by Auger Electron Spectroscopy (AES)*; EAG Laboratories, 2019.
(39) Auger Electron Spectroscopy (AES) Surface Analysis Technique. https://www.phi.com/surface-analysis-techniques/aes.html (accessed July 19, 2021).
(40) Abdelmageed, G.; Mackeen, C.; Hellier, K.; Jewell, L.; Seymour, L.; Tingwald, M.; Bridges, F.; Zhang, J. Z.; Carter, S. Effect of Temperature on Light Induced Degradation in Methylammonium Lead Iodide Perovskite Thin Films and Solar Cells. *Sol. Energy Mater. Sol. Cells* **2018**, *174*, 566−571.
(41) X-ray Photoelectron Spectroscopy (XPS) Reference Pages: What is Adventitious Carbon?.
(42) Hou, C.-H.; Hung, S.-H.; Jhang, L.-J.; Chou, K.-J.; Hu, Y.-K.; Chou, P.-T.; Su, W.-F.; Tsai, F.-Y.; Shieh, J.; Shyue, J.-J. Validated Analysis of Component Distribution Inside Perovskite Solar Cells and Its Utility in Unveiling Factors of Device Performance and Degradation. *ACS Appl. Mater. Interfaces* **2020**, *12*, 22730−22740.

https://doi.org/10.1021/acsomega.1c05002
ACS Omega 2021, 6, 34606−34614